Volume 13
Number 47
21 December 2021
Pages 19695-20310

Nanoscale

rsc.li/nanoscale

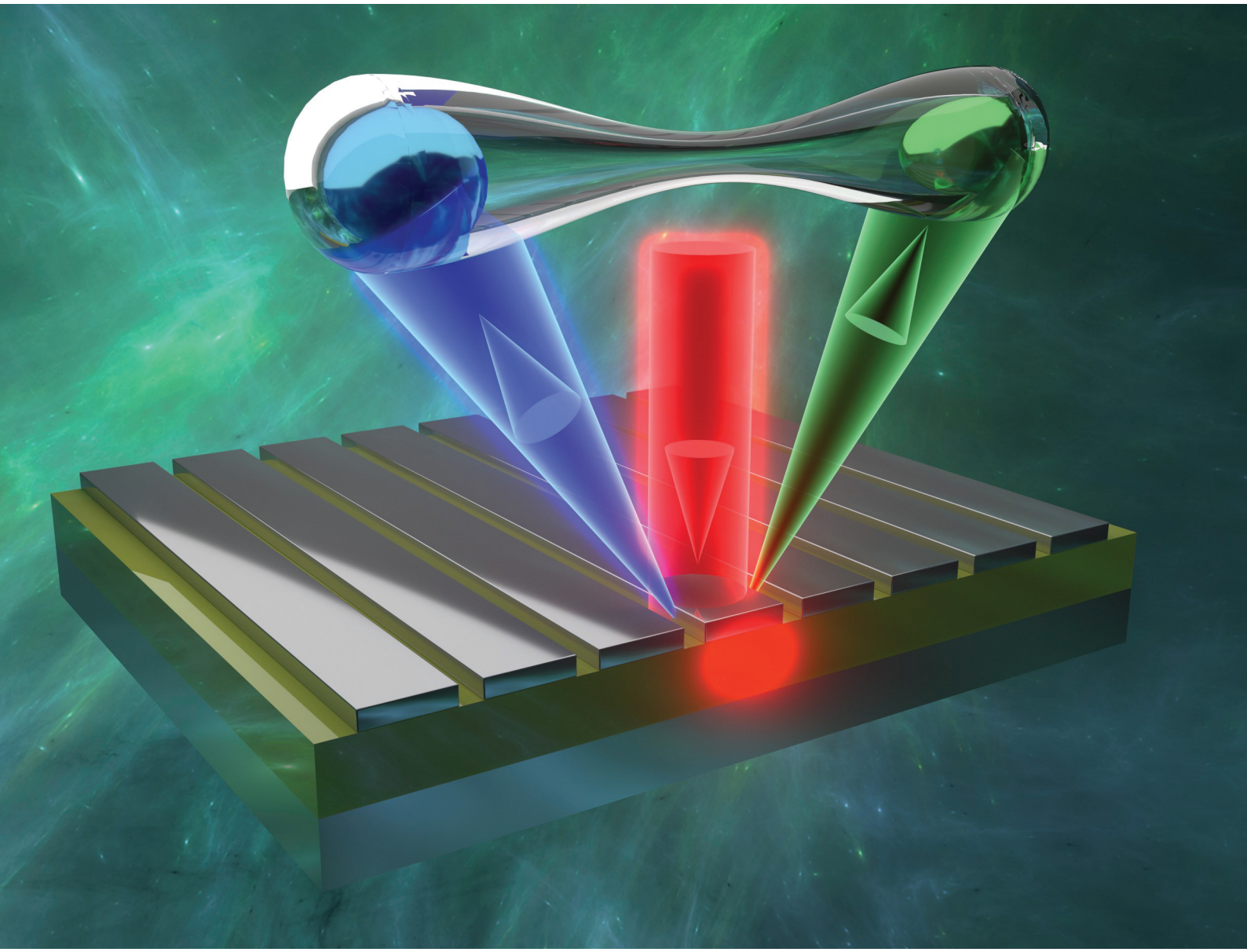

ISSN 2040-3372

ROYAL SOCIETY OF CHEMISTRY

PAPER
Christos Argyropoulos *et al.*
Efficient single-photon pair generation by spontaneous parametric down-conversion in nonlinear plasmonic metasurfaces

NCNST

Nanoscale

ROYAL SOCIETY OF CHEMISTRY

PAPER

View Article Online
View Journal | View Issue

Check for updates

Cite this: *Nanoscale*, 2021, **13**, 19903

Efficient single-photon pair generation by spontaneous parametric down-conversion in nonlinear plasmonic metasurfaces†

Boyuan Jin, Dhananjay Mishra and Christos Argyropoulos *

Received 16th August 2021,
Accepted 19th October 2021

DOI: 10.1039/d1nr05379e

rsc.li/nanoscale

Spontaneous parametric down-conversion (SPDC) is one of the most versatile nonlinear optical techniques for the generation of entangled and correlated single-photon pairs. However, it suffers from very poor efficiency leading to extremely weak photon generation rates. Here we propose a plasmonic metasurface design based on silver nanostripes combined with a bulk lithium niobate ($LiNbO_3$) crystal to realize a new scalable, ultrathin, and efficient SPDC source. By coinciding fundamental and higher order resonances of the metasurface with the generated signal and idler frequencies, respectively, the electric field in the nonlinear media is significantly boosted. This leads to a substantial enhancement in the SPDC process which, subsequently, by using the quantum-classical correspondence principle, translates to very high photon-pair generation rates. The emitted radiation is highly directional and perpendicular to the metasurface in contrast to relevant dielectric structures. The incorporation of circular polarized excitation further increases the photon-pair generation efficiency. The presented work will lead to the design of new efficient ultrathin SPDC single-photon nanophotonic sources working at room temperature that are expected to be critical components in free-space quantum optical communications. In a more general context, our findings can have various applications in the emerging field of quantum plasmonics.

1. Introduction

The field of quantum photonics is poised to have a broad range of emerging applications spanning ultrafast speed and robust security quantum communications,[1–8] rapid and accurate quantum computations,[9–16] and high resolution metrology, imaging, and sensing.[17–20] The generation of high-quality entangled single-photon pairs by nonclassical light sources is an essential building block for the majority of these applications and has been a long-sought goal in modern quantum optical technologies.[21,22] The process of spontaneous parametric down-conversion (SPDC), alternatively known as parametric fluorescence, in a nonlinear crystal is one of the most versatile techniques for the generation of entangled and correlated single-photon pairs.[23–30] However, as a typical spontaneous quantum nonlinear process, it suffers from extremely poor efficiency due to the very weak nature of nonlinear quantum optical processes.[31] Recently, extensive efforts have been devoted to boost this effect by utilizing conventional designs based on nonlinear crystals,[32] waveguides,[33,34] photonic crystals,[35] and ring resonators[36,37] that are usually bulky or unsuitable for free-space applications.

In contrast, metasurfaces[8] that can sustain subwavelength confined gap-plasmons are promising novel ultrathin designs to realize saleable and efficient SPDC sources, as they can tightly confine the incident optical power locally in ultrasmall nanoscale volumes resulting in enhanced nonlinear optical effects.[38–44] Thus, the SPDC photon-pair generation rate process, which is proportional to the local pump intensity and induced field enhancement, is expected to be substantially improved by these compact plasmonic configurations. Recently, the SPDC process has been enhanced by using a single dielectric cylindrical nanoantenna.[45] The extension of this configuration to antenna arrays is expected to further boost its output signal but remains elusive. In addition, despite the low optical loss of this dielectric nanoantenna, its photon-pair generation rate is limited mainly due to the low field enhancement along its geometry leading to relative weak nonlinear light–matter interactions. Interestingly, most of the configurations presented in the literature, employed to enhance SPDC, use III–V semiconductor materials due to their large second-order nonlinearity.[31] However, it is very challenging for the majority of these designs to obtain emitted photon pairs in the normal direction to the sample's surface combined with enhanced single-photon pair generation rate

Department of Electrical and Computer Engineering, University of Nebraska-Lincoln, Lincoln, Nebraska 68588, USA. E-mail: christos.argyropoulos@unl.edu

†Electronic supplementary information (ESI) available. See DOI: 10.1039/d1nr05379e

while operating as a free-standing configuration (not waveguide).

In this work, we resolve these problems by designing a new plasmonic nonlinear metasurface to efficiently generate entangled single-photon pairs. The metasurface can sustain a loosely confined gap-plasmon mode and is composed of periodic silver nanostripes placed on top of a homogeneous lithium niobate ($LiNbO_3$) spacer layer with the whole structure terminated by a silver substrate. $LiNbO_3$ has relatively strong second-order nonlinearity which can be of great potential in SPDC applications. However, it is usually used in elongated bulky waveguide configurations exhibiting relatively low SPDC efficiency.[46–49] In the currently proposed structure, the induced localized surface and gap plasmon modes generate extremely strong electric field enhancement around the edges of the silver nanostripes and, in particular, in the nanogap region. The bottom silver substrate works as a perfect reflector which creates loosely confined gap plasmons due to the induced Fabry–Pérot resonances in the nanogap that further enhance the electric field in the $LiNbO_3$ nonlinear spacer layer. The generated electric field enhancement hotspots coincide with the metasurface second-order nonlinear materials, mainly $LiNbO_3$ and to a lesser extend the silver–dielectric interface.

To achieve the maximum entangled photon-pair generation rate due to the boosted SPDC process, the metasurface resonances coincide with both generated signal and idler frequencies. Note that the SPDC process is usually complicated and requires random variables to be characterized due to its pure quantum nature. To decrease the computational complexity of the current problem, we simulate the reverse classical nonlinear process, named sum-frequency generation (SFG), and then employ the quantum-classical correspondence relationship to calculate the photon-pair generation rate, in a similar way to various previous works relevant to different SPDC systems.[45,50,51] It is demonstrated that the photon-pair generation rate in the proposed nonlinear metasurface is substantially increased compared to the current state-of-the-art designs with equivalent ultrathin profiles operating as free-standing structures (not as waveguides). We thoroughly investigate the factors that affect the obtained efficient SPDC process, such as operation frequency, incident wave polarization, and photon emission angles. The various media comprising the proposed metasurface and consisting the main sources of the SPDC process strength are also explored. The proposed new ultrathin SPDC metasurface design works in reflection mode and generates a spatially narrow photon emission beam perpendicular to its surface. It also has high efficiency and can be used at room temperature, which are major advantages compared to alternative solid-state single photon emitters that usually operate at cryogenic temperatures.[22] Moreover, it can easily be made frequency tunable by varying its geometry, making it possible to work at various input and output generated wavelengths. Its versatile and efficient SPDC response is ideal to be used in vital components of various emerging free-space quantum optical devices. The presented generation of high-quality entangled single-photon pairs can find a plethora of interesting applications in the emerging field of quantum plasmonics.

2. Nonlinear metasurface to boost the SPDC process

SPDC is generated from the spontaneous parametric amplification of vacuum thermal noise photons in a nonlinear medium when pumped at low enough power to avoid any stimulated photon generation.[30] It can lead to the spontaneous generation of two correlated and entangled photons at the angular frequencies ω_s and ω_i, respectively, following the annihilation of a pump photon at frequency ω_p. The subscripts s, i, and p represent the signal, idler, and pump photons, respectively, and the conservation of energy $\omega_p = \omega_s + \omega_i$ is always satisfied. The process is schematically shown in the inset of Fig. 1a. SPDC is restricted from the phase-matching condition (*i.e.*, combined conservation of energy and momentum) which is the most typical limitation for any nonlinear optical process.[31]

The proposed nonlinear plasmonic metasurface design is schematically shown in Fig. 1. Periodic silver nanostripes are placed on top of a $LiNbO_3$ spacer layer and terminated by a silver substrate. The thickness, width, and periodicity of the silver nanostripes are: b = 100 nm, l = 450 nm, and a = 560 nm, respectively. The edges of the silver nanostripes are rounded with a radius r = 2 nm to imitate experimental fabrication imperfections.[39] The thickness of the $LiNbO_3$ layer is chosen to be h = 306 nm after optimization with the goal to tune the fundamental and higher order resonances to the involved waves, as it will be shown later. Note that similar thickness $LiNbO_3$ layers have been experimentally verified in various recent papers[52–54] and were recently grown over a metal bottom reflector,[55] similar to the currently proposed configuration. The illumination used to excite the current structure is always a plane wave with the electric field parallel to the x-direction or, equivalently, transverse magnetic (TM) polarization. The nanostripe metasurface will be polarization dependent and will not work for the transverse electric (TE) polarization. However, it can become polarization independent without altering its performance if the nanostripes are replaced by an array of three-dimensional (3D) nanocube resonators[43] that are polarization insensitive.

Localized surface plasmons are formed at the metasurface fundamental and higher-order resonances leading to the generation of extremely strong electric fields around the edges of the silver nanostripes and in the nanogap. Furthermore, the bottom silver substrate operates as a reflector, forming a loosely confined gap-plasmon mode due to an additional Fabry–Pérot resonance that further increases the electric field in the $LiNbO_3$ spacer layer. The proposed metasurface works only in reflection mode and the transmission is zero due to the thick bottom silver substrate. The reflectance spectrum in the linear operation of the proposed metasurface is computed

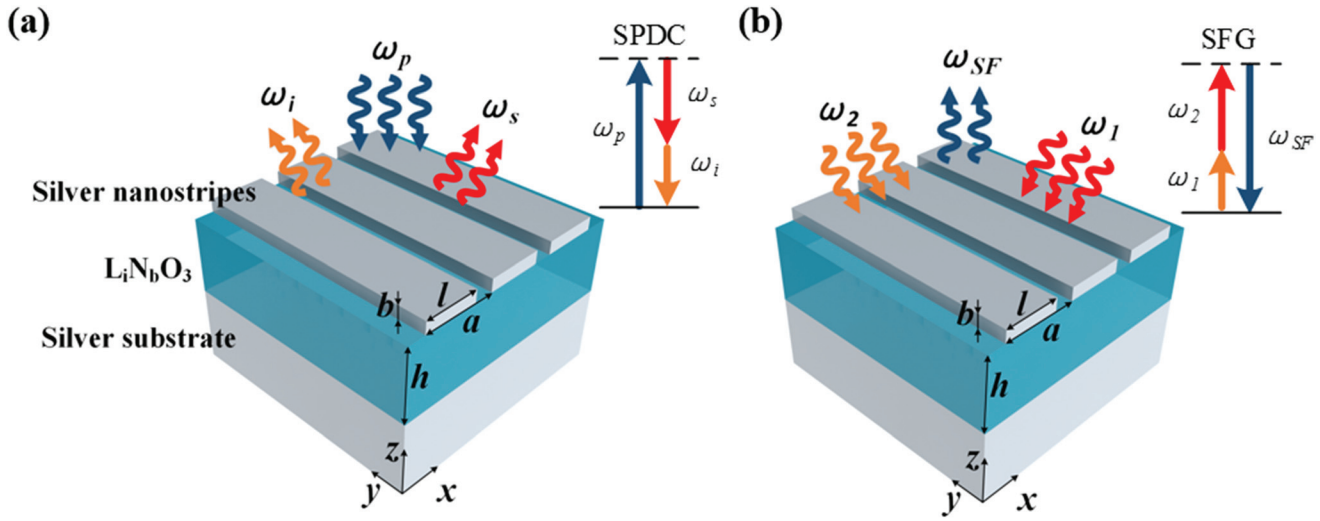

Fig. 1 Schematics of the proposed nonlinear plasmonic metasurface made of silver nanostripes, lithium niobate spacer layer, and silver substrate. The metasurface can boost both (a) quantum SPDC and (b) classical SFG processes, which are schematically shown in the insets of (a) and (b), respectively.

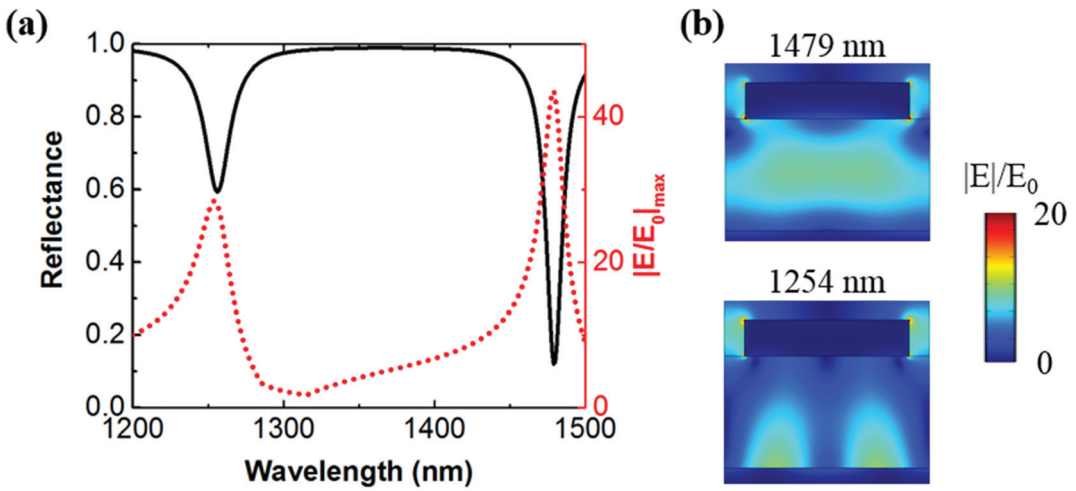

Fig. 2 (a) Linear reflectance and the maximum electric field enhancement in the $LiNbO_3$ layer as functions of the wavelength. (b) Electric field enhancement distribution at the fundamental (up) and higher-order (bottom) resonances.

under normal incident illumination and shown in Fig. 2a. The obtained reflectance dips suggest that the metasurface has two resonance modes in the near-infrared (IR) spectrum, both accompanied by large field enhancement $|E/E_0|$, where E is the local electric field, E_0 is the amplitude of the incident field, and $|E/E_0|_{max}$ is the maximum field enhancement. The electric field is substantially boosted in the $LiNbO_3$ layer and along the silver nanostripe and substrate surfaces, as shown in Fig. 2b. These consist of the main second-order nonlinear materials of the proposed metasurface. It is well known that the generally weak nonlinear materials need to be excited by intense optical input intensities.[56,57] Hence, the local electric field enhancement achieved by the current plasmonic metasurface is critical for improving its efficiency.[41,58] This principle is general and can be applied to both stimulated and spontaneous nonlinear processes, including the currently studied SPDC. As a result, it is expected that if we coincide λ_i and λ_s with the fundamental (1479 nm) and higher-order (1254 nm) resonances, respectively, of the current nonlinear metasurface design, the efficiency of the SPDC process will be substantially improved.

Structures designed to enhance classical second-order nonlinear processes can also be used to enhance the purely quantum optical SPDC process. Indeed, it has been proven that there is a quantum-classical correspondence between the SPDC and SFG processes, respectively, based on the Green's function formalism.[45,50,51] More specifically, the number of photon pairs generated through SPDC are proportional to the SFG conversion efficiency, while the pump waves (ω_1 and ω_2)

and the generated sum-frequency wave ($\omega_{SF} = \omega_1 + \omega_2$) of the classical SFG process propagate in the opposite directions to the signal (ω_s), idler (ω_i), and pump (ω_p) photons in the SPDC process.[45,50,51] The SFG process is schematically shown in the inset of Fig. 1b. The quantum-classical correspondence concept is also shown in Fig. 1 and can be applied to any system that is reciprocal in the linear regime, allowing to predict the efficiency of the SPDC generated entangled photon pairs by studying the classical SFG nonlinear process under reversed direction interacting waves. In this case, the entangled photon-pair generation rate due to the quantum SPDC process is given by the formula:[45]

$$\frac{dN_{pair}}{dt} = 2\pi c \frac{\lambda_p^4}{\lambda_s^5 \lambda_i^3} \frac{I_p \Delta\lambda_s}{A} \eta_{SFG}, \quad (1)$$

where λ_p, λ_i, and λ_s are the wavelengths of the pump, idler, and signal photons, respectively, c is the light speed in vacuum, I_p is the SPDC incident pump wave intensity, and A is the illumination area along the metasurface. The photon-pair rate is proportional to the bandwidth of the generated signal $\Delta\lambda_s$. Since the SPDC is a spontaneous effect, all the combinations of λ_i and λ_s that satisfy the relation $\omega_p = \omega_s + \omega_i$ will be produced from noise photons generated by quantum vacuum fluctuations.[59] Therefore, $\Delta\lambda_s$ in eqn (1) is determined by the spectral response of the structure and, even more importantly, the bandwidth of the detector. Finally, $\eta_{SFG} = P_{SF}/I_1/I_2$ represents the efficiency of the corresponding classical SFG nonlinear process, where P_{SF} is the power outflow of the generated sum-frequency wave due to the SFG process, and I_1 and I_2 are the incident intensities of the SFG pump waves. Note that strong field enhancement is not required at the pump frequency of the SPDC process to increase the single-photon pair generation rate efficiency, as it is predicted by eqn (1). It can also be detrimental to the SPDC process because it can lead to stimulated photon generation.[30] The measured P_{SF} always depends on the illumination area A along the sample. However, we normalize the calculated photon-pair generation rate to the sample's surface A by dividing this area on the right side of eqn (1). In addition, the photon-pair generation rate is proportional to the incident pump intensity I_p and the efficiency of the corresponding SFG process η_{SFG}. However, as we will show later, η_{SFG} is independent of the incident intensities I_1 and I_2. To improve the η_{SFG} and thus enhance the SPDC process, the nanophotonic structure of the sample needs to be carefully designed and optimized.

We avoid the complicated quantum calculations involved in the SPDC process by utilizing the quantum-classical correspondence and studying the easier to model classical SFG process. Hence, our study is simplified to the investigation of a nonlinear plasmonic metasurface design that can exhibit exceptionally strong SFG response. The SFG conversion efficiency is calculated by using nonlinear full-wave simulations based on the finite element method (FEM) software COMSOL Multiphysics. These electromagnetic simulations are not trivial, since the linear Maxwell's equations need to be substantially modified in COMSOL by introducing a nonlinear polarizability to model the SFG nonlinear process in the nanoscale. More details about the linear and nonlinear modeling are provided in the ESI.† [60] Periodic boundary conditions are used and only one unit cell of the nanostripe plasmonic metasurface is modeled. Moreover, considering that the length of the silver nanostripes is much longer than the currently used near-IR wavelengths, the structure is modeled as two-dimensional (2D), which substantially decreases the computational speed and memory burden of the computationally demanding nonlinear simulations. It should also be noted that the linear permittivities of silver and $LiNbO_3$ used in the simulations have practical values taken from the experiment data.[61,62]

$LiNbO_3$ is an emerging and currently widely used bulk nonlinear material due to its relatively strong second-order nonlinearity.[46–49] The three orthogonal components of the induced anisotropic nonlinear polarizability in the SFG process are given by:[45,63]

$$P_x^{NL} = 2\varepsilon_0[d_{33}E_{1_x}E_{2_x} + d_{31}(E_{1_y}E_{2_y} + E_{1_z}E_{2_z})], \quad (2)$$

$$P_y^{NL} = 2\varepsilon_0\left[d_{31}(E_{1y}E_{2x} + E_{1x}E_{2y}) + d_{22}(E_{1y}E_{2y} - E_{1z}E_{2z})\right], \quad (3)$$

$$P_z^{NL} = 2\varepsilon_0\left[d_{31}(E_{1_z}E_{2_x} + E_{1_x}E_{2_z}) - d_{22}(E_{1_y}E_{2_z} + E_{1_z}E_{2_y})\right], \quad (4)$$

where ε_0 is the permittivity of free space, and d_{31} = 5.95 pm V^{-1}, d_{33} = 34.4 pm V^{-1}, and d_{22} = 3.07 pm V^{-1} are the non-zero elements of the $LiNbO_3$ crystal anisotropic second-order nonlinear susceptibilities.[31,64] The subscripts x, y, and z in eqn (2)–(4) represent the corresponding components of the induced nonlinear polarizability and electric field along different axes. Due to the non-centrosymmetric crystalline structure of $LiNbO_3$, its second-order nonlinear response is anisotropic and relatively high. This is in contrast to centrosymmetric crystals that, in principle, cannot have a second-order nonlinear response.[31] In order to utilize the predominant d_{33} nonlinear $LiNbO_3$ susceptibility in the current scenario of x-polarized incident waves, the crystalline optical axis of $LiNbO_3$ in our design is aligned along the x-direction. In III–V semiconductor materials, such as gallium arsenide (GaAs) and aluminum gallium arsenide (AlGaAs), which are also non-centrosymmetric but have stronger second-order susceptibilities, the SFG frequency mixing process is mainly pronounced when the polarization directions of the two input waves are orthogonal.[45,65] This specific property of III–V semiconductor nanostructures makes them challenging to generate sum-frequency radiation collinear to the incident waves.[45,63,66] Since normal incident inputs are preferable in most applications, the generated sum-frequency radiation and, consequently, SPDC entangled single-photon pairs from III–V semiconductor materials usually cannot be perpendicular to the sample surface. In contrast, $LiNbO_3$ achieves the highest SFG conversion efficiency when the inputs are parallel polarized. Thus, the generated sum-frequency wave can be easily emitted perpendicular to the currently proposed nonlinear plasmonic metasurface. This is another major advantage of the currently proposed free-standing efficient SPDC source compared to

various relevant designs based on elongated photonic waveguide structures. In addition, the presented plasmonic metasurface can also compensate the relatively small (compared to semiconductors) nonlinear susceptibilities of $LiNbO_3$. As we will show later, the photon-pair generation rate in our proposed plasmonic metasurface is several times larger compared to AlGaAs nanoantennas[45] despite the larger nonlinear susceptibility of AlGaAs compared to the currently used $LiNbO_3$.

Note that enhanced second-order nonlinear effects can also be generated at the metal–dielectric interface,[67–70] in addition to the bulk $LiNbO_3$ nonlinear material. This surface second-order nonlinearity originates from the asymmetry of the neighboring different atoms at the interface. Due to the ultrathin interface region, this surface nonlinearity is more accurate and convenient to be modeled by a boundary condition, similar to 2D nonlinear materials, such as graphene.[71–73] The tangential component of the surface SFG polarizability $P_{s_\parallel}^{NL}$ gives rise to a surface current density $J_{s_\parallel}^{NL}$, but is one-order of magnitude smaller than the normal component $P_{s_\perp}^{NL}$.[74,75] Therefore, $P_{s_\parallel}^{NL}$ is usually assumed to be negligible for simplicity. Here, the subscript s represents "surface". On the other hand, $\mathbf{P}_{s_\perp}^{NL} = 2\varepsilon_0\chi_{s_\perp}^{(2)}E_{1_\perp}E_{2_\perp}\hat{\mathbf{r}}_\perp$ results in a discontinuity of $E_\parallel$ at the interface,[76] where $\hat{\mathbf{r}}_\perp$ is the unit vector normal to the interface, and $E_{1_\perp}$ and $E_{2_\perp}$ are the normal components in the metal region of the two input fields, respectively. This surface source generated by $P_{s_\perp}^{NL}$ can be modeled as an equivalent surface magnetic current density $\mathbf{J}_{m,s}^{NL} = \hat{\mathbf{r}}_\perp \times (\nabla_\parallel P_{s_\perp}^{NL})/\varepsilon'$,[76] where ε' is the permittivity of the adjacent dielectric material, and $\nabla_\parallel$ is the gradient operator on the tangential direction. Note that $\chi_{s_\perp}^{(2)}$ is the overall surface component of the bulk nonlinear susceptibility $\chi_b^{(2)}$ due to the minor penetration depth of light in the metal. Theoretically, $\chi_{s_\perp}^{(2)}$ can be expressed as $\chi_{s_\perp}^{(2)} = h_{eff}\chi_b^{(2)}$, where h_{eff} is the effective thickness of the metal–dielectric interface.[77] However, the value of $\chi_{s_\perp}^{(2)}$ can also be derived from experimental measurements without knowing the values of $\chi_b^{(2)}$ and h_{eff}.[78,79] In this work, we use $\chi_{s_\perp,Ag}^{(2)} = 1.59 \times 10^{-18}\ m^2\ V^{-1}$ for silver according to relevant reported experimental data.[74,77,80] This value is extremely low, especially compared to lithium niobate, since silver is a centrosymmetric material, and does not play a substantial role in the SFG process, as it will be shown in the next section.

3. Significantly boosted SFG process

We characterize the SFG process strength by computing the conversion efficiency $CE_{SFG} = P_{SF}/(P_1 + P_2)$, where P_{SF} is the power outflow of the generated sum-frequency wave, and $(P_1 + P_2)$ is the total input power from both pump waves.[81,82] As shown by the red dashed line in Fig. 2a, the electric field is greatly boosted at the resonant wavelengths of the proposed plasmonic metasurface. When the input pump waves operate at λ_1 and λ_2 wavelengths that are chosen to vary close to the metasurface two resonance modes (1254 nm and 1479 nm, respectively), the computed SFG conversion efficiency is shown in Fig. 3a and takes relatively high values. The intensities of the incident waves are both fixed to a moderate value of 100 MW cm^{-2}, which ensures that the sample will not be affected by detrimental thermal effects and eventually destroyed (melt) by heating. Pulsed lasers can be used to improve the heat dissipation. Interestingly, even higher input intensity values were used before in other nonlinear experiments based on similar plasmonic metasurfaces without causing damage to the sample.[39] Moreover, the undepleted-pump approximation is always adopted in all SFG simulations, since the generated wave is much weaker compared to the input waves.

The maximum conversion efficiency can exceed 1.8×10^{-6} in the case of $\lambda_1 = 1257$ nm and $\lambda_2 = 1477$ nm, leading to a generated sum-frequency wave at the visible wavelength $\lambda_{SF} = 679$ nm. The SFG conversion efficiency also depends on the input intensity, as shown in Fig. 3b, when plotted at the same wavelengths, suggesting that even higher conversion efficiency values can be achieved just by increasing the input power. The proposed metasurface realizes high conversion efficiency that is comparable (or even improved) to different previously reported structures with dramatically enhanced second-order nonlinearity.[83,84] We also investigate the distinct contribution of each nonlinear material involved in the metasurface design. As shown by the red dashed line in Fig. 3b, the reduction in the conversion efficiency is minor to non-existent if the nonlinearity of the silver–dielectric interface is neglected ($\chi_{sAg}^{(2)} = 0$). Although the field enhancement on the metal surface is extremely large, it is derived that the dominant contribution in the second-order nonlinear process is mainly from the $LiNbO_3$ layer. When the silver nanostripes are removed from the metasurface, the conversion efficiency is substantially decreased by five orders of magnitude, as shown by the blue dashed line in Fig. 3b. Hence, the nanocavities formed by the geometry of the presented structure are crucial to achieve substantially enhanced nonlinear operation.

As discussed before, nonlinear metasurfaces made of III–V semiconductor materials are difficult to radiate the sum-frequency generated wave perpendicular to the sample surface. To investigate the directivity of our proposed metasurface, Fig. 4 shows the computed far field radiation pattern of one unit cell, where θ_1 and θ_2 are the incident angles of the two input pump waves, respectively. Under normal ($\theta_1 = \theta_2 = 0°$) or symmetrically oblique ($\theta_1 = -\theta_2$) illumination, most of the generated power of the sum-frequency wave is directionally reflected to free space normal to the metasurface. It is also clear that the nonlinearly generated radiation decreases under small oblique incident angle illumination. More details about the far field calculations are provided in the ESI.†[60]

Due to the anisotropic nature of the $\chi^{(2)}$ tensor in the involved nonlinear materials and the structure's polarization sensitivity, the generated sum-frequency radiation will be affected by the input wave polarization. In the case of linear polarization, we define the orthogonal- (O) and parallel- (P) polarizations when the incident plane wave electric field $\boldsymbol{E}_0$ is

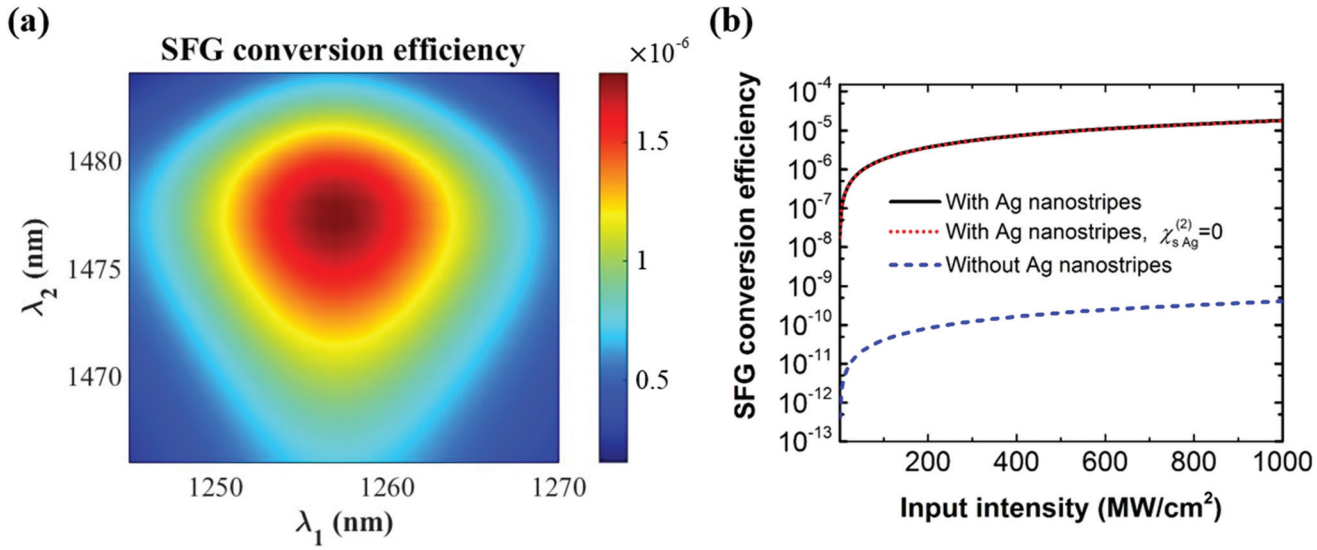

Fig. 3 (a) SFG conversion efficiency as a function of the two pump wave incident wavelengths. (b) SFG conversion efficiency as a function of the pump wave incident intensity for three different cases: (i) all nonlinear materials included (black), (ii) silver–dielectric interface nonlinearity removed (red), and (iii) silver nanostripes removed from the metasurface design (blue).

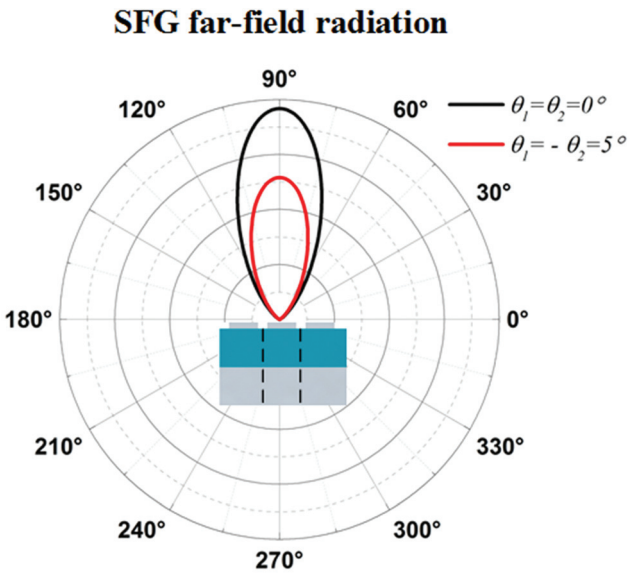

Fig. 4 SFG far-field radiation pattern from the metasurface under normal ($\theta_1 = \theta_2 = 0°$) and oblique ($\theta_1 = -\theta_2 = 5°$) incidence illumination.

orthogonal (TM polarization) or parallel (TE polarization) to the silver nanostripes. The SFG conversion efficiency is computed and presented in Fig. 5a under different combinations of incident polarizations including O or P, and, additionally, right- and left-handed circular polarizations (RCP and LCP, respectively). The input waves are always normally incident to the metasurface with intensities $I_1 = I_2 = 100$ MW cm^{-2}. When either one of the two incident pump waves is P-polarized, it can be seen in Fig. 5a that the generated sum-frequency power is extremely low and close to zero. This is because the metasurface resonance performance is polarization sensitive, *i.e.*, it cannot resonate under P-polarization, and thus the field cannot be enhanced in the metasurface nanogap. In any other combination, the radiation at the sum-frequency is strong. The conversion efficiency shown in Fig. 5a is computed only for the O-polarized sum-frequency power outflow $\left(0.5 \times \mathrm{Re}\left[-H^{*}_{\mathrm{SF},y} E_{\mathrm{SF},x}\right]\right)$, since the y-component of the sum-frequency electric field $E_{\mathrm{SF},y}$ is much lower and can be neglected for any polarized excitation. This suggests that the generated sum-frequency wave has purely linear polarization with the electric field along the x-direction (O-polarized). Interestingly, the angular-dependent polarization state of the sum-frequency generated wave can be derived by the SFG far-field radiation pattern shown in Fig. 4. The power of the sum-frequency nonlinearly generated wave is maximum at normal emission angles and abruptly decreases as the emission angles deviate from normal. The pattern shown in Fig. 4 has always the same shape even in the case of different angle incident wave illuminations. In addition, the y-component of the electric field of the sum-frequency nonlinearly generated wave is always very low compared to the x-component for different angles of emission even off the normal emission angle. As a result, the generated sum-frequency wave will be linearly polarized with the electric field along the x-direction, which however will have much lower amplitude as the emission angles increase and deviate compared to normal. This is mainly due to the resonance mode that is angle-dependent and can be perfectly excited only for normal incident waves.

It is interesting that circular polarization can generate even stronger SFG, as clearly shown in Fig. 5a. In fact, the relative SFG strength between linear and circular polarized input pump waves depends on the operation frequency. For example,

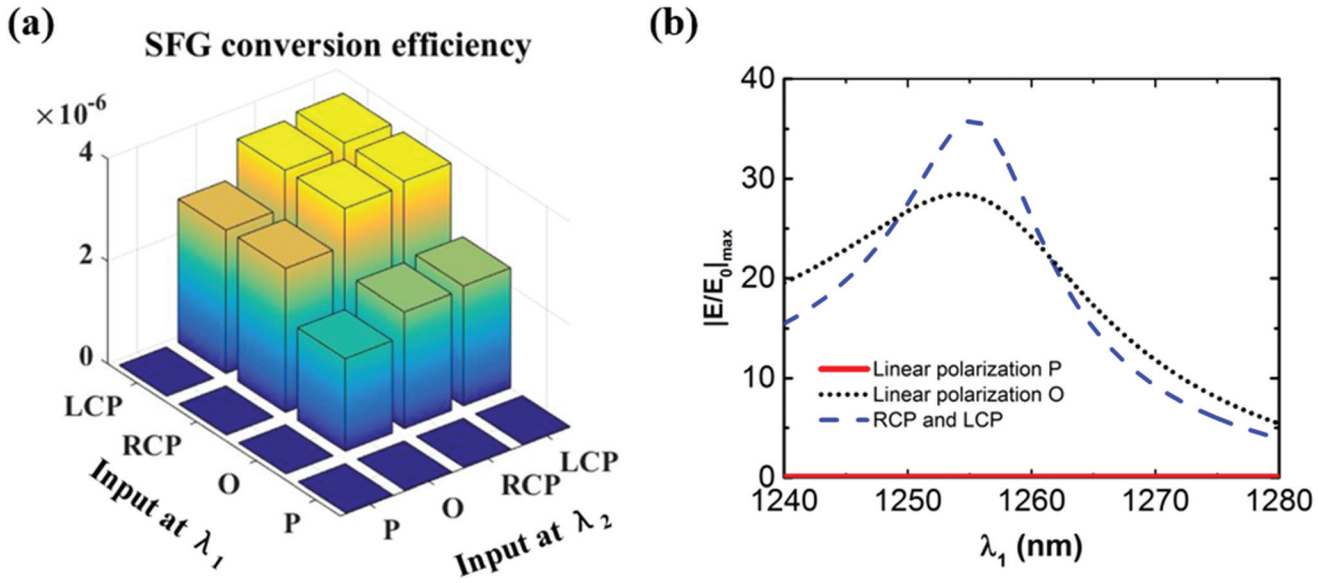

Fig. 5 (a) SFG conversion efficiency under different combinations of the input pump wave polarizations; O and P: linearly polarized with electric field E_0 orthogonal and parallel to the silver nanostripes, respectively; LCP and RCP: left- and right-handed circularly polarized, respectively. (b) The maximum field enhancement in the $LiNbO_3$ layer as a function of the pump wavelength λ_1 for different polarizations.

Fig. 5b shows the maximum field enhancement in the $LiNbO_3$ layer as a function of λ_1 for different polarizations operating in the linear regime. It can be seen that the field enhancement for both circular polarizations at the resonance is larger compared to the linear polarization, since magnetic modes are excited in the nanogap region that couples more efficiently to circular polarized incident waves.[85–88] In the ESI,† [60] we also compute the linear reflectance spectra when the plasmonic metasurface is excited by circular polarized waves, where it is shown in Fig. S1† that both reflection dips are deeper compared to those under linear polarized excitation. In addition, we clearly demonstrate the magnetic nature of the excited resonance modes by computing the magnetic field enhancement distributions in Fig. S2.† [60] This suggests that the SFG under RCP and/or LCP polarized pump input beams will be stronger at the resonance wavelength compared to the linearly polarized pump waves. In contrast, linear O-polarized pump waves can generate stronger SFG at off-resonance frequencies, where they can produce a larger electric field than the RCP and LCP inputs, as shown in Fig. 5b. The field enhancement for the P-polarized input waves is also shown by the red solid line in Fig. 5b and is always extremely small and less than one when varying λ_1. As was mentioned before, plasmonic resonances cannot be excited under P-polarization with the current nanostripe-based metasurface, resulting in negligible SFG efficiency under this polarization. However, we should note that the relationship $|E/E_0|_{max}$ is only a coarse indicator to characterize the SFG strength. To be more accurate, the SFG conversion efficiency is proportional to $\iiint P^{NL} dV$, where P^{NL} is given by eqn (2)–(4) presented in the previous section that include the $LiNbO_3$ anisotropy. To conclude, the SFG nonlinear process is substantially enhanced by the current nonlinear plasmonic metasurface when illuminated by either O^- or circular polarized pump waves.

4. Highly efficient photon-pair generation due to enhanced SPDC

Based on the SFG simulations presented in the previous section, we extract the power outflow of the generated sum frequency wave along the unit cell of our proposed metasurface, named P_{SF}, and compute the SFG efficiency η_{SFG} by dividing P_{SF} with the incident intensities I_1 and I_2 of the pump waves. Unlike the SFG conversion efficiency (CE_{SFG}) used before, the η_{SFG} metric is independent of the incident intensities and can only be enhanced by the nanophotonic structure. The photon-pair generation rate in the reversed SPDC process is computed by using the quantum-classical correspondence defined before by eqn (1). We assume that the metasurface is illuminated uniformly by a perpendicularly incident plane wave, also known as the pump (λ_p). In eqn (1), we assume that the sample area A is approximately mm^2 scale. Thus, the derived photon-pair generation rate is for a 1 mm^2 metasurface and has units of Hz mm^{-2}. In addition, the metasurface photon-pair generation rate is proportional to the bandwidth of the generated signal and the input pump intensity. Therefore, to make the comparison more convenient, we normalize the computed photon-pair generation rate to the signal bandwidth $\Delta\lambda_s$ = 1 nm and the used pump intensity I_p = 1 W cm^{-2}. The pump intensity I_p = 1 W cm^{-2} used in our computations is extremely low compared to typical nonlinear applications to avoid any stimulated photon generation. Moreover, the excitation electric field enhancement in the nanogap at the pump signal (λ_p) has a

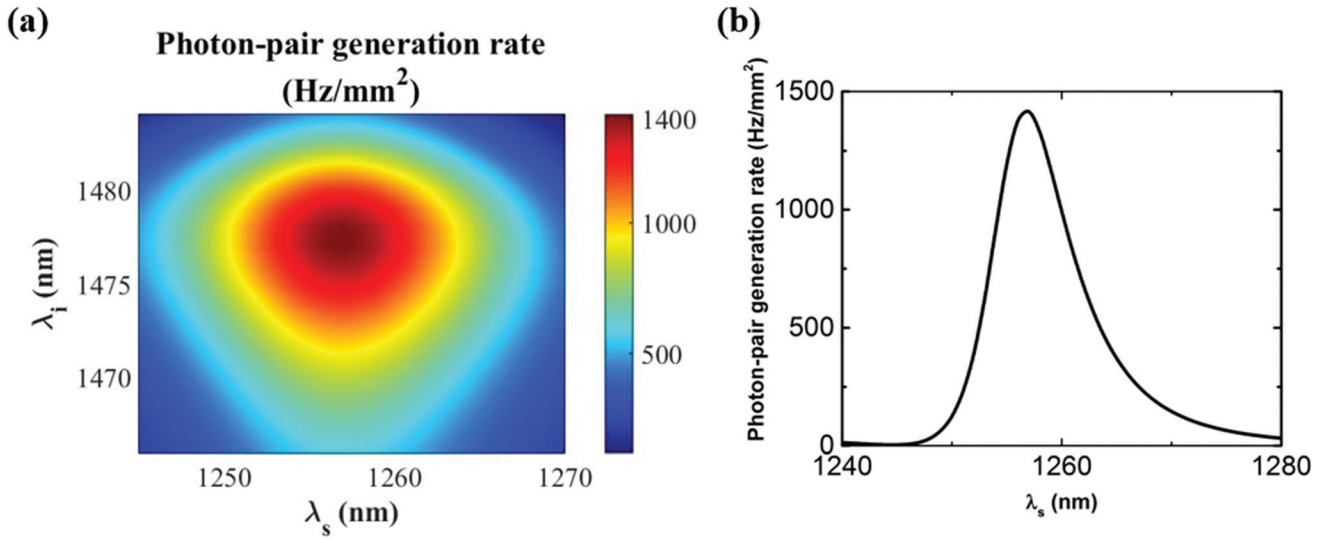

Fig. 6 (a) Photon-pair generation rate of the proposed nonlinear plasmonic metasurface as a function of the signal and idler wavelengths. (b) Photon-pair generation rate as a function of the signal wavelength when the pump wavelength is kept constant at λ_p = 679 nm.

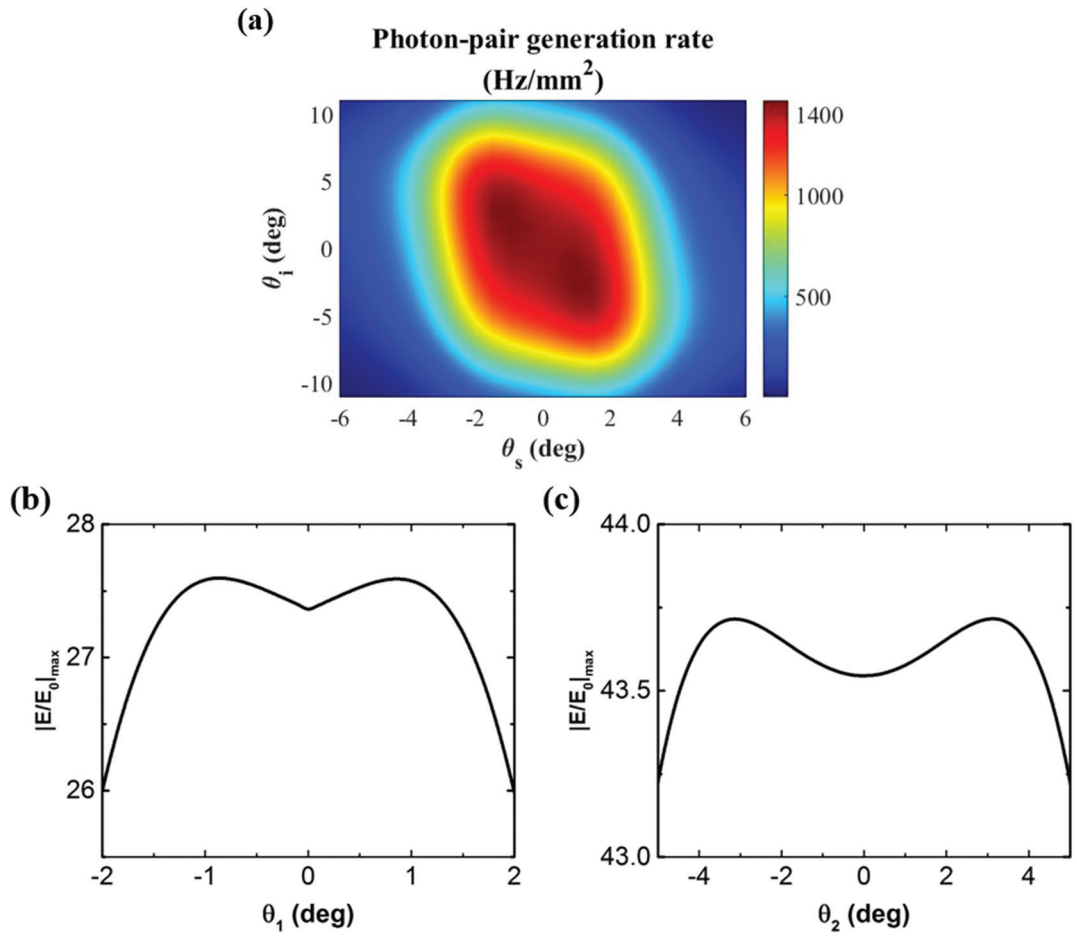

Fig. 7 (a) Photon-pair generation rate due to the boosted SPDC process as a function of the signal and idler wave observation angles (θ_s and θ_i). (b–c) The maximum electric field enhancement in the $LiNbO_3$ layer as a function of (b) θ_1 and (c) θ_2 in the classical counterpart of the SPDC process, *i.e.,* SFG.

much lower value compared to the electric field enhancement at the metasurface resonances shown in Fig. 2(a). The computed photon-pair generation rate of our proposed metasurface as a function of the signal and idler wavelengths is shown in Fig. 6a. When we vary both signal and idler waves close to the resonant wavelengths of the proposed plasmonic metasurface, the photon-pair generation rate can reach a very high value of approximately 1400 Hz mm^{-2}. Currently, the best state-of-the-art ultrathin designs based on alternative nanoantenna or metasurface structures can only generate photon pairs with an estimated rate of approximately 400 Hz mm^{-2} or 72 Hz mm^{-2}, respectively.[45,89] Hence, the proposed nonlinear plasmonic metasurface can significantly increase the photon-pair generation rate. This rate can be even further increased if the $LiNbO_3$ spacer layer becomes thinner, which will lead to stronger electric field enhancement and, as a result, increased nonlinear light–matter interactions. According to the quantum-classical correspondence, the extremely high photon-pair generation rate occurs for the following visible and near-IR wavelengths: λ_p = 679 nm, λ_s = 1257 nm, and λ_i = 1477 nm. The computed photon-pair generation rate as a function of the signal wavelength is also shown in Fig. 6b, where the pump is fixed to λ_p = 679 nm. This plot proves that the enhanced photon generation is indeed due to the resonances excited by the metasurface. The maximum photon-pair generation rate is obtained at λ_s = 1257 nm, which coincides with the metasurface's higher-order resonance.

The quantum-classical correspondence also implies that the input pump wave (λ_p) to achieve the enhanced SPDC process should be O-polarized. In addition, the generated signal and idler stream of photons are largely concentrated in the normal direction with respect to the metasurface. Indeed, Fig. 7 shows the photon-pair generation rate at different observation angles (θ_s and θ_i) for the signal and idler waves, where θ_s and θ_i are defined with respect to the metasurface's normal direction. The used wavelengths are λ_p = 679 nm, λ_s = 1257 nm, and λ_i = 1477 nm. It is obvious that the radiated signal and idler photon power is restricted in a solid angle of few degrees around the normal direction. In addition, it is interesting that the direction with the maximum radiation power is not precisely normal to the sample surface. This can be explained again by studying the classical counterpart of the SFG process, where Fig. 7b and c show the maximum field enhancement in the $LiNbO_3$ layer as a function of the two pump wave incident angles. It can be seen that the peak field enhancement occurs when the input waves are slightly off the normal incidence. The incident angles (θ_1 and θ_2) of the peak field enhancement in the classical SFG process directly correspond to the observation angles (θ_s and θ_i) of the photon-pair generation in the quantum SPDC process.

5. Conclusions

In summary, a compact nonlinear plasmonic metasurface is proposed to efficiently generate entangled and correlated photon pairs. By coinciding the metasurface fundamental and higher-order resonances with both the generated signal and idler frequencies, the electric field in the nonlinear media is significantly enhanced leading to a substantially boosted classical SFG nonlinear process that directly corresponds to an efficient quantum SPDC process. It is demonstrated that the metasurface design can effectively improve the efficiency of both SFG and SPDC processes due to strongly enhanced nonlinear light–matter interactions. The $LiNbO_3$ layer consists of the dominant contribution in the second-order nonlinear process. The SPDC emitted streams of photons are highly directional and perpendicular to the metasurface plane. This out-of-plane directionality property overcomes the in-plane emission limitation of all-dielectric nanostructures, mainly due to the crystalline properties of III–V semiconductor materials, leading to an easier detection of the generated entangled photon pairs. The effect of polarization is also investigated because of the anisotropic nature of the presented second-order nonlinear response. The proposed free-standing SPDC source provides high efficiency, room temperature operation, out-of-plane directionality, and tunable response that can be further altered by changing the metasurface geometry or using different input and output wavelengths. Novel versatile quantum optical devices are envisioned based on the presented metasurface design that can be especially useful for free-space quantum plasmonic and other nanophotonic applications.

Conflicts of interest

There are no conflicts to declare.

Acknowledgements

This work was partially supported by the NSF Nebraska Materials Research Science and Engineering Center (Grant No. DMR-1420645), the Office of Naval Research Young Investigator Program (ONR-YIP) (Grant No. N00014-19-1-2384), the National Science Foundation/EPSCoR RII Track-1: Emergent Quantum Materials and Technologies (EQUATE) (under Grant No. OIA-2044049), and the Jane Robertson Layman Fund from the University of Nebraska Foundation.

References

1 N. Gisin, *et al.*, Quantum cryptography, *Rev. Mod. Phys.*, 2002, **74**(1), 145–195.
2 J. L. O'Brien, A. Furusawa and J. Vuckovic, Photonic quantum technologies, *Nat. Photonics*, 2009, **3**(12), 687–695.
3 B. Hensen, *et al.*, Loophole-free Bell inequality violation using electron spins separated by 1.3 kilometres, *Nature*, 2015, **526**(7575), 682–686.

4 T. B. Hoang, *et al.*, Ultrafast spontaneous emission source using plasmonic nanoantennas, *Nat. Commun.*, 2015, **6**, 7788.
5 Y. Li, A. Nemilentsau and C. Argyropoulos, Resonance energy transfer and quantum entanglement mediated by epsilon-near-zero and other plasmonic waveguide systems, *Nanoscale*, 2019, **11**(31), 14635–14647.
6 Y. A. Chen, *et al.*, An integrated space-to-ground quantum communication network over 4,600 kilometres, *Nature*, 2021, **589**(7841), 214.
7 M. Pompili, *et al.*, Realization of a multinode quantum network of remote solid-state qubits, *Science*, 2021, **372**(6539), 259.
8 A. S. Solntsev, G. S. Agarwal and Y. Y. Kivshar, Metasurfaces for quantum photonics, *Nat. Photonics*, 2021, **15**(5), 327–336.
9 D. Deutsch, Quantum-Theory, the church-turing principle and the universal quantum computer, *Proc. R. Soc. London, Ser. A*, 1985, **400**(1818), 97–117.
10 S. Lloyd, Universal quantum simulators, *Science*, 1996, **273**(5278), 1073–1078.
11 E. Knill, R. Laflamme and G. J. Milburn, A scheme for efficient quantum computation with linear optics, *Nature*, 2001, **409**(6816), 46–52.
12 G. Vidal, Efficient classical simulation of slightly entangled quantum computations, *Phys. Rev. Lett.*, 2003, **91**(14), 147902.
13 R. Jozsa and N. Linden, On the role of entanglement in quantum-computational speed-up, *Proc. R. Soc. A*, 2003, **459**(2036), 2011–2032.
14 R. Prevedel, *et al.*, High-speed linear optics quantum computing using active feed-forward, *Nature*, 2007, **445**(7123), 65–69.
15 S. Wehner, D. Elkouss and R. Hanson, Quantum internet: A vision for the road ahead, *Science*, 2018, **362**(6412), eaam9288.
16 S. Daiss, *et al.*, A quantum-logic gate between distant quantum-network modules, *Science*, 2021, **371**(6529), 614–617.
17 J. Dowling, A. Gatti and A. Sergienko, Special issue: Quantum imaging - Preface, *J. Mod. Opt.*, 2006, **53**(5–6), 573–574.
18 V. Giovannetti, S. Lloyd and L. Maccone, Quantum metrology, *Phys. Rev. Lett.*, 2006, **96**(1), 010401.
19 S. Lloyd, Enhanced sensitivity of photodetection via quantum illumination, *Science*, 2008, **321**(5895), 1463–1465.
20 J. F. Barry, *et al.*, Optical magnetic detection of single-neuron action potentials using quantum defects in diamond, *Proc. Natl. Acad. Sci. U. S. A.*, 2016, **113**(49), 14133–14138.
21 M. Barbieri, *et al.*, Qubit-programmable operations on quantum light fields, *Sci. Rep.*, 2015, **5**, 15125.
22 P. Senellart, G. Solomon and A. White, High-performance semiconductor quantum-dot single-photon sources, *Nat. Nanotechnol.*, 2017, **12**(11), 1026–1039.
23 P. G. Kwiat, *et al.*, New high-intensity source of polarization-entangled photon pairs, *Phys. Rev. Lett.*, 1995, **75**(24), 4337–4341.
24 P. G. Kwiat, *et al.*, Ultrabright source of polarization-entangled photons, *Phys. Rev. A*, 1999, **60**(2), R773–R776.
25 S. Fasel, *et al.*, High-quality asynchronous heralded single-photon source at telecom wavelength, *New J. Phys.*, 2004, **6**, 163.
26 A. B. U'Ren, *et al.*, Efficient conditional preparation of high-fidelity single photon states for fiber-optic quantum networks, *Phys. Rev. Lett.*, 2004, **93**(9), 093601.
27 S. Azzini, *et al.*, Ultra-low power generation of twin photons in a compact silicon ring resonator, *Opt. Express*, 2012, **20**(21), 23100–23107.
28 G. Harder, *et al.*, An optimized photon pair source for quantum circuits, *Opt. Express*, 2013, **21**(12), 13975–13985.
29 Q. Li, M. Davanco and K. Srinivasan, Efficient and low-noise single-photon-level frequency conversion interfaces using silicon nanophotonics, *Nat. Photonics*, 2016, **10**(6), 406–414.
30 O. Slattery, *et al.*, Background and review of cavity-enhanced spontaneous parametric down-conversion, *J. Res. Natl. Inst. Stand. Technol.*, 2019, **124**, 124019.
31 R. W. Boyd, *Nonlinear optics*, Academic Press, New York, 2008.
32 C. Couteau, Spontaneous parametric down-conversion, *Contemp. Phys.*, 2018, **59**(3), 291–304.
33 X. Cheng, *et al.*, Design of spontaneous parametric down-conversion in integrated hybrid SixNy-PPLN waveguides, *Opt. Express*, 2019, **27**(21), 30773–30787.
34 P. B. Main, P. J. Mosley and A. V. Gorbach, Spontaneous parametric down-conversion in asymmetric couplers: Photon purity enhancement and intrinsic spectral filtering, *Phys. Rev. A*, 2019, **100**(5), 053815.
35 V. Introini, *et al.*, Spontaneous parametric down conversion in a doubly resonant one-dimensional photonic crystal, *Opt. Lett.*, 2020, **45**(5), 1244–1247.
36 M. Akbari and A. A. Kalachev, Third-order spontaneous parametric down-conversion in a ring microcavity, *Laser Phys. Lett.*, 2016, **13**(11), 1–5.
37 J. Schneeloch, *et al.*, Introduction to the absolute brightness and number statistics in spontaneous parametric down-conversion, *J. Opt.*, 2019, **21**(4), 043501.
38 C. Argyropoulos, C. Ciraci and D. R. Smith, Enhanced optical bistability with film-coupled plasmonic nanocubes, *Appl. Phys. Lett.*, 2014, **104**(6), 063108.
39 J. B. Lassiter, *et al.*, Third-harmonic generation enhancement by film-coupled plasmonic stripe resonators, *ACS Photonics*, 2014, **1**(11), 1212–1217.
40 Z. Q. Huang, *et al.*, Optical bistability with film-coupled metasurfaces, *Opt. Lett.*, 2015, **40**(23), 5638–5641.
41 B. Jin and C. Argyropoulos, Enhanced four-wave mixing with nonlinear plasmonic metasurfaces, *Sci. Rep.*, 2016, **6**(1), 28746.

42 F. Ding, *et al.*, A review of gap-surface plasmon metasurfaces: fundamentals and applications, *Nanophotonics*, 2018, **7**(6), 1129–1156.
43 J. J. Baumberg, *et al.*, Extreme nanophotonics from ultrathin metallic gaps, *Nat. Mater.*, 2019, **18**(7), 668–678.
44 Q. X. Shen, *et al.*, Active control of multiple, simultaneous nonlinear optical processes in plasmonic nanogap cavities, *ACS Photonics*, 2020, **7**(4), 901–907.
45 G. Marino, *et al.*, Spontaneous photon-pair generation from a dielectric nanoantenna, *Optica*, 2019, **6**(11), 1416–1422.
46 D. Bonneau, *et al.*, Fast path and polarization manipulation of telecom wavelength single photons in lithium niobate waveguide devices, *Phys. Rev. Lett.*, 2012, **108**(5), 053601.
47 H. Jin, *et al.*, On-chip generation and manipulation of entangled photons based on reconfigurable lithium-niobate waveguide circuits, *Phys. Rev. Lett.*, 2014, **113**(10), 103601.
48 Y. Ming, *et al.*, Tailoring entanglement through domain engineering in a lithium niobate waveguide, *Sci. Rep.*, 2014, **4**, 4812.
49 R. Luo, *et al.*, On-chip second-harmonic generation and broadband parametric down-conversion in a lithium niobate microresonator, *Opt. Express*, 2017, **25**(20), 24531–24539.
50 A. N. Poddubny, I. V. Iorsh and A. A. Sukhorukov, Generation of photon-plasmon quantum states in nonlinear hyperbolic metamaterials, *Phys. Rev. Lett.*, 2016, **117**(12), 123901.
51 F. Lenzini, *et al.*, Direct characterization of a nonlinear photonic circuit's wave function with laser light, *Light: Sci. Appl.*, 2018, **7**, 17143.
52 F. Zhang, *et al.*, Ultrafast all-optical tunable Fano resonance in nonlinear metamaterials, *Appl. Phys. Lett.*, 2013, **102**(18), 181109.
53 C. Wang, *et al.*, Metasurface-assisted phase-matching-free second harmonic generation in lithium niobate waveguides, *Nat. Commun.*, 2017, **8**, 2098.
54 Y. S. Lin, *et al.*, Metasurface color filters using aluminum and lithium niobate configurations, *Nanoscale Res. Lett.*, 2020, **15**(1), 77.
55 Z. H. Chen, *et al.*, Grating coupler on lithium niobate thin film waveguide with a metal bottom reflector, *Opt. Mater. Express*, 2017, **7**(11), 4010–4017.
56 B. Jin and C. Argyropoulos, Nonreciprocal transmission in nonlinear PT–symmetric metamaterials using epsilon–near–zero media doped with defects, *Adv. Opt. Mater.*, 2019, **7**(23), 1901083.
57 B. Jin and C. Argyropoulos, Self-induced passive nonreciprocal transmission by nonlinear bifacial dielectric metasurfaces, *Phys. Rev. Appl.*, 2020, **13**(5), 054056.
58 S. A. H. Gangaraj, *et al.*, Broadband field enhancement and giant nonlinear effects in terminated unidirectional plasmonic waveguides, *Phys. Rev. Appl.*, 2020, **14**(5), 054061.
59 G. P. Agrawal, *Nonlinear fiber optics*, Academic, San Diego, 2007.
60 ESI† provides details of the numerical method used to simulate the linear response and nonlinear SFG process and the linear response of the metasurface when excited by circular polarized incident waves.
61 P. B. Johnson and R. W. Christy, Optical constants of the noble metals, *Phys. Rev. B: Solid State*, 1972, **6**(12), 4370–4379.
62 D. E. Zelmon, D. L. Small and D. Jundt, Infrared corrected Sellmeier coefficients for congruently grown lithium niobate and 5 mol% magnesium oxide-doped lithium niobate, *J. Opt. Soc. Am. B*, 1997, **14**(12), 3319–3322.
63 A. Fedotova, *et al.*, Second-harmonic generation in resonant nonlinear metasurfaces based on lithium niobate, *Nano Lett.*, 2020, **20**(12), 8608–8614.
64 J. C. Lindon, G. E. Tranter and D. Koppenaal, *Encyclopedia of spectroscopy and spectrometry*, Academic Press, 2016.
65 X. Q. Zhang, *et al.*, Sum frequency generation in pure zinc-blende GaAs nanowires, *Opt. Express*, 2013, **21**(23), 28432–28437.
66 L. Carletti, *et al.*, Controlling second-harmonic generation at the nanoscale with monolithic AlGaAs-on-AlOx antennas, *Nanotechnology*, 2017, **28**(11), 114005.
67 C. Ciraci, *et al.*, Second-harmonic generation in metallic nanoparticles: Clarification of the role of the surface, *Phys. Rev. B: Condens. Matter Mater. Phys.*, 2012, **86**(11), 115451.
68 S. Raza, *et al.*, Nonlocal optical response in metallic nanostructures, *J. Phys.: Condens. Matter*, 2015, **27**(18), 183204.
69 J. Butet, P. F. Brevet and O. J. F. Martin, Optical second harmonic generation in plasmonic nanostructures: from fundamental principles to advanced applications, *ACS Nano*, 2015, **9**(11), 10545–10562.
70 N. C. Panoiu, *et al.*, Nonlinear optics in plasmonic nanostructures, *J. Opt.*, 2018, **20**(8), 083001.
71 B. Jin, T. Guo and C. Argyropoulos, Enhanced third harmonic generation with graphene metasurfaces, *J. Opt.*, 2017, **19**(9), 094005.
72 T. Guo, B. Jin and C. Argyropoulos, Hybrid graphene-plasmonic gratings to achieve enhanced nonlinear effects at terahertz frequencies, *Phys. Rev. Appl.*, 2019, **11**(2), 024050.
73 T. Guo and C. Argyropoulos, Recent advances in terahertz photonic technologies based on graphene and their applications, *Adv. Photonics Res.*, 2021, 2000168.
74 D. Krause, C. W. Teplin and C. T. Rogers, Optical surface second harmonic measurements of isotropic thin-film metals: Gold, silver, copper, aluminum, and tantalum, *J. Appl. Phys.*, 2004, **96**(7), 3626–3634.
75 J. Makitalo, S. Suuriniemi and M. Kauranen, Boundary element method for surface nonlinear optics of nanoparticles, *Opt. Express*, 2011, **19**(23), 23386–23399.
76 K. N. Reddy, *et al.*, Revisiting the boundary conditions for second-harmonic generation at metal-dielectric interfaces, *J. Opt. Soc. Am. B*, 2017, **34**(9), 1824–1832.
77 M. Weismann and N. C. Panoiu, Theoretical and computational analysis of second- and third-harmonic generation in periodically patterned graphene and transition-metal

dichalcogenide monolayers, *Phys. Rev. B*, 2016, **94**(3), 035435.

78 W. E. Angerer, *et al.*, Ultrafast second-harmonic generation spectroscopy of GaN thin films on sapphire, *Phys. Rev. B: Condens. Matter Mater. Phys.*, 1999, **59**(4), 2932–2946.

79 C. W. Teplin and C. T. Rogers, Experimental example of isotropic surface second-harmonic generation: dc-sputtered air-exposed aluminum thin films, *Phys. Rev. B: Condens. Matter Mater. Phys.*, 2002, **65**(24), 245408.

80 L. Dalstein, *et al.*, Nonlinear optical response of a gold surface in the visible range: A study by two-color sum-frequency generation spectroscopy. I. Experimental determination, *J. Chem. Phys.*, 2018, **148**(13), 134701.

81 Z. Z. Hao, *et al.*, Sum-frequency generation in on-chip lithium niobate microdisk resonators, *Photonics Res.*, 2017, **5**(6), 623–628.

82 H. Kerdoncuff, *et al.*, Cavity-enhanced sum-frequency generation of blue light with near-unity conversion efficiency, *Opt. Express*, 2020, **28**(3), 3975–3984.

83 F. Wang, A. B. F. Martinson and H. Harutyunyan, Efficient nonlinear metasurface based on nonplanar plasmonic nanocavities, *ACS Photonics*, 2017, **4**(5), 1188–1194.

84 X. N. Ye, *et al.*, Sum-frequency generation in lithium-niobate-on-insulator microdisk via modal phase matching, *Opt. Lett.*, 2020, **45**(2), 523–526.

85 A. Pors, M. G. Nielsen and S. I. Bozhevolnyi, Broadband plasmonic half-wave plates in reflection, *Opt. Lett.*, 2013, **38**(4), 513–515.

86 A. Pors, M. G. Nielsen and S. I. Bozhevolnyi, Analog computing using reflective plasmonic metasurfaces, *Nano Lett.*, 2015, **15**(1), 791–797.

87 Z. Q. Miao, *et al.*, Widely tunable terahertz phase modulation with gate-controlled graphene metasurfaces, *Phys. Rev. X*, 2015, **5**(4), 041027.

88 Y. W. Huang, *et al.*, Gate-tunable conducting oxide metasurfaces, *Nano Lett.*, 2016, **16**(9), 5319–5325.

89 T. Santiago-Cruz, *et al.*, Photon Pairs from Resonant Metasurfaces, *Nano Lett.*, 2021, **21**(10), 4423–4429.

